Acta Crystallographica Section A
**Foundations of Crystallography**
ISSN 0108-7673

Received 23 May 2009
Accepted 16 February 2010

# Interference fringes in multiple Bragg–Laue mode and mirage fringes from bent crystals

**Tomoe Fukamachi,[a]* Masahiko Tohyama,[a] Kenji Hirano,[a] Masami Yoshizawa,[a] Riichirou Negishi,[a] Dongying Ju,[a] Keiichi Hirano[b] and Takaaki Kawamura[c]**

[a]Saitama Institute of Technology, 1690 Fusaiji, Fukaya, Saitama 369-0293, Japan, [b]Institute of Material Structure Science, KEK-PF, High Energy Accelerator Research Organization, Oho, Tsukuba, Ibaraki 305-0801, Japan, and [c]Department of Mathematics and Physics, University of Yamanashi, Kofu, Japan. Correspondence e-mail: tomoe@sit.ac.jp

Interference fringes are measured in the diffraction from the surface as well as from the lateral surface of an Si single-crystal strip which is deformed in cantilever bending as a function of the tip displacement. The interference fringes are observed only when the bending strain is applied. Both interference fringes change conspicuously by increasing the bending strain. The number of the interference fringes changes, and the positions and heights of the peaks in the fringes change. These variations can be explained by the change of the interference between the beams in multiple Bragg–Laue modes and those of mirage diffraction based on the dynamical theory of diffraction.

## 1. Introduction

Interference fringes were observed in X-ray diffraction from the lateral surface of a Ge single-crystal strip in a multiple Bragg–Laue mode (Fukamachi *et al.*, 2004, 2005). The interference fringes are caused by interference between the internal beams in the Bragg–Laue (BL) mode and those in the Bragg–Bragg–Laue (BBL) mode when the incident beam is regarded as a spherical wave (Hirano *et al.*, 2008, 2009*a*,*b*). In these studies the diffraction is measured when the linear absorption coefficient $\mu$ is minimized as a result of the dynamical (Borrmann) effect and the path length of X-rays is quite large. According to the dynamical theory, when $\mu$ is minimized the angle $\gamma$ between the diffraction plane and the actual propagation direction of the wavefield varies from zero to the Bragg angle $\theta_B$ (Yoshizawa *et al.*, 2008; Hirano *et al.*, 2008, 2009*a*,*b*). The propagating direction is given by the direction of the Poynting vector $\mathbf{S}$ (we call the beam corresponding to $\mathbf{S}$ the 'refracted beam') whose direction does not coincide with either the diffracted beam direction or the transmitted beam direction.

Some X-ray beam paths in multiple BL diffraction modes are shown in Fig. 1. The angle $\gamma$ is defined in order to specify the glancing angle between the incident surface and the direction of the incident beam as shown in Fig. 1(*a*). In the range $\gamma < \gamma_1 = \tan^{-1}(H/L)$, the beam corresponding to $\mathbf{S}_1$ directly reaches the lateral surface (BL mode). Here $H$ is the crystal thickness and $L$ is the distance between the incident point of X-rays and the crystal edge. In the range $\gamma_1 \le \gamma \le \gamma_2 = \tan^{-1}(2H/L)$, the beam corresponding to $\mathbf{S}_2$ reaches the back surface first. Then a part of the beam is reflected and reaches the lateral surface (BBL mode), and the rest of it is transmitted through the back surface.

In a crystal with a constant strain gradient, the ray trajectories of $\mathbf{S}_1$, $\mathbf{S}_2$ and $\mathbf{S}_3$ are shown in Figs. 1(*b*) and 1(*c*). In

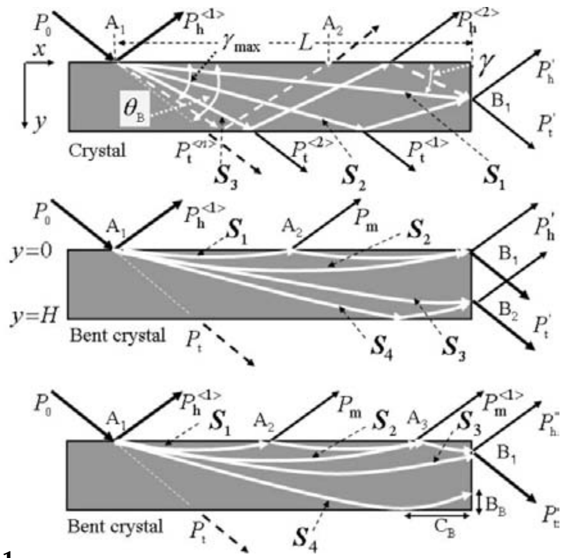

**Figure 1**
Schematic illustration of the beam geometry in multiple BL modes. $\theta_B$ is the Bragg angle, $\gamma$ the angle between the diffraction plane and the direction of the refracted beam, $H$ the crystal thickness and $L$ the distance between the incident point of the X-ray and the edge of the crystal. The beam geometries are (*a*) in an unbent crystal, (*b*) in a weakly bent crystal and (*c*) in a crystal bent more strongly. $P_h^{\langle 1\rangle}$ represents the intensity of the diffracted beam from $A_1$ (the incident point) and $P_h^{\langle 2\rangle}$ represents the intensity of the beam coming out of the crystal at $A_2$ after reflection from the back surface. $P_t^{\langle 1\rangle}$ and $P_t^{\langle 2\rangle}$ represent the intensities of the transmitted beams from the refracted beams $\mathbf{S}_2$ and $\mathbf{S}_3$, respectively. $P_h'$ and $P_t'$ represent the intensities of diffraction from the lateral surface in the diffracted and transmitted beam directions. $P_m$ and $P_m^{\langle 1\rangle}$ represent the intensities of the mirage diffraction and the mirage fringe from the bent crystal.

doi:10.1107/S0108767310006148

Fig. 1(*b*), since the path of the refracted beam $\mathbf{S}_1$ is a branch of a hyperbola (Gronkowski & Malgrange, 1984; Authier, 2001), the beam corresponding to $\mathbf{S}_1$ intersects the crystal surface at $\mathrm{A}_2$. A part of the beam is reflected and reaches the lateral surface, while the rest of it contributes to the diffracted beam coming out of the crystal at $\mathrm{A}_2$ on the surface. We call the latter diffraction 'mirage diffraction'. Relationships between the mirage diffraction and elastically bent crystal with a constant strain gradient have been investigated by Yan & Noyan (2006) and Yan *et al.* (2007), who theoretically analysed the measured diffraction by using the wavefield.

At $\mathrm{A}_3$ in Fig. 1(*c*), interference fringes are caused by the interference between the two refracted beams $\mathbf{S}_1$ and $\mathbf{S}_2$. We call these interference fringes 'mirage fringes'. It is noted that mirage fringes are different from mirage diffraction. The mirage fringes are caused by the interference between two mirage diffraction beams. In Bragg section topographs of a bent crystal, Chukhovskii & Petrashen' (1988) studied interferometric fringes caused by this interference. As X-ray trajectories change in a bent crystal, it is expected that interference fringes in the diffraction from the lateral surface of a bent crystal are quite different from those of the unbent crystal.

In this paper we report on the measured variations of interference fringes in diffraction from the lateral surface in the multiple BL mode as a function of bending strain and the comparison of them with the mirage fringes from the surface of the crystal.

## 2. Experiments

The sample was an Si strip, 40 mm long, 10 mm wide and 0.099 mm thick. It was clamped at one end. The other end could be deflected to a known displacement $D$ by the cantilever tip through a micrometer drive as shown in Fig. 2.

The measuring system is schematically shown in Fig. 3. The experiments were carried out by using X-rays from synchrotron radiation at bending-magnet beamline BL-15C of the Photon Factory, KEK, Tsukuba, Japan. The X-rays were incident on the sample crystal in the direction normal to the bent direction (Fig. 2). The X-rays were $\sigma$-polarized and were monochromated using an Si 111 double-crystal monochromator. The X-ray energy was 11100 ± 0.5 eV. The vertical and horizontal beam widths after slit 1 were adjusted to be 30 µm and 1000 µm, respectively. The transmitted ($P_\mathrm{t}$) and diffracted ($P_\mathrm{h}$) intensities as well as the diffraction intensities from the lateral surface in the transmitted ($P'_\mathrm{t}$) and diffracted ($P'_\mathrm{h}$) beam directions were recorded on the nuclear plate (ILFORD L4, emulsion thickness 25 µm) and were measured using scintillation counters. The distance $L$ was varied between 890 and 940 µm depending on the displacement $D$. The distance from the lateral surface of the crystal to the nuclear plate was 17 mm.

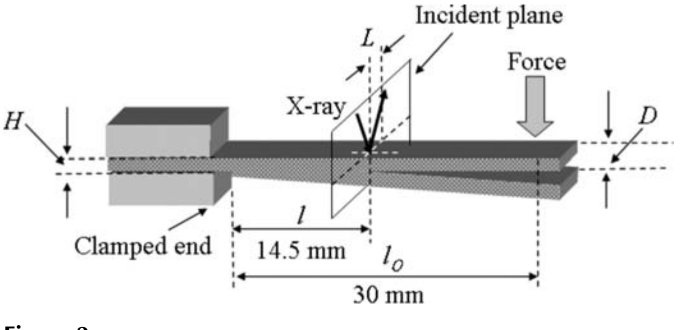

**Figure 2**
Sample and bending jig geometries. The X-rays are incident along the direction normal to the bending direction.

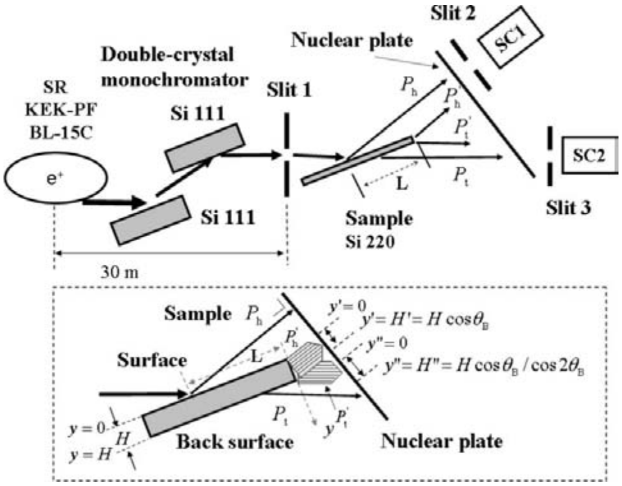

**Figure 3**
Schematic diagram of the measuring system. SR stands for the synchrotron radiation X-ray source and SC the scintillation counter. The inset shows a magnification of the region around the sample crystal.

## 3. Experimental results

Fig. 4 shows photographs of diffracted patterns of $P_\mathrm{h}$, $P'_\mathrm{h}$ (left), $P_\mathrm{t}$ and $P'_\mathrm{t}$ (right) recorded on the nuclear plate when the

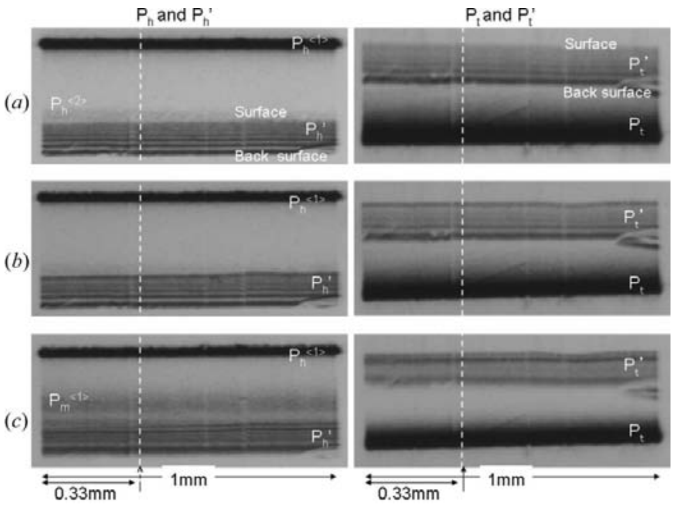

**Figure 4**
Photographs of $P_\mathrm{h}$ and $P'_\mathrm{h}$ on the left, and $P_\mathrm{t}$ and $P'_\mathrm{t}$ on the right. The displacement $D$ is (*a*) 0 µm, (*b*) 10 µm and (*c*) 50 µm. The measured distance $L$ is 940 µm in (*a*) and (*b*), and 890 µm in (*c*).

intensities of $P_{\rm h}'$ were maximum. Here, (*a*) shows photographs from the unbent crystal, while (*b*) and (*c*) show those from the bent crystal. The cantilever-tip displacement $D$ is 10 µm in (*b*) and 50 µm in (*c*). The interference fringes are observed in both diffraction patterns of $P_{\rm h}'$ and $P_{\rm t}'$ from the lateral surface. In Fig. 4(*a*) the fringes in $P_{\rm h}'$ and $P_{\rm t}'$ on the back surface side are clearly seen but the fringes on the surface side are blurred. In Fig. 4(*b*) the fringes in $P_{\rm h}'$ and $P_{\rm t}'$ are clearly seen both on the surface side and on the back surface side. In Fig. 4(*c*), two intensity maxima on the surface side are clearly seen. A weak wide band (as indicated by $P_{\rm h}^{\langle 2\rangle}$) is seen in the upper part of $P_{\rm h}'$ in Fig. 4(*a*). This band is caused by the diffracted beam through $A_2$ on the surface after reflection at the back surface as shown in Fig. 1(*a*). A wide band (as indicated by $P_{\rm m}^{\langle 1\rangle}$) is seen in the upper part of $P_{\rm h}'$ in Fig. 4(*c*), which is caused by the interference between two mirage diffraction beams in the $\rm B\overline{B}^2$ mode and in the $\rm B\overline{B}$ mode shown in Fig. 1(*c*). Here $\overline{\rm B}$ stands for the mirage diffraction in the Bragg mode.

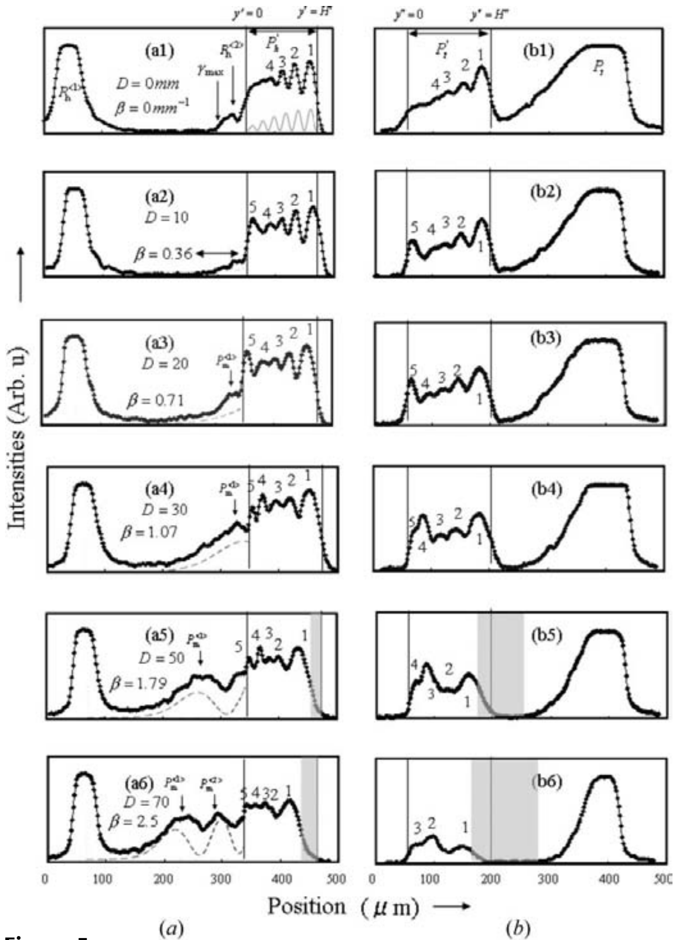

**Figure 5**
Intensity profiles (linear scale) of $P_{\rm h}$ and $P_{\rm h}'$ in (*a*), and $P_{\rm t}$ and $P_{\rm t}'$ in (*b*). The displacement $D$ is (1) 0, (2) 10, (3) 20, (4) 30, (5) 50 and (6) 70 µm. The diamonds are measured intensities. The dashed lines from (*a*3) to (*a*6) are calculated intensities of mirage fringes. The thin solid line in (*a*1) shows calculated intensities of the interference between the beam in the BL mode and the beam in the BBL mode according to the method of Hirano *et al.* (2009*a*,*b*). The absorption effect is taken into account. The grey regions in (*a*5)–(*a*6) and (*b*5)–(*b*6) correspond to the dark regions shown in Fig. 1(*c*). $P_{\rm m}^{\langle 1\rangle}$ in (*a*5), $P_{\rm m}^{\langle 1\rangle}$ and $P_{\rm m}^{\langle 2\rangle}$ in (*a*6) represent peak intensities of the mirage fringe.

Fig. 5 shows the intensity profiles recorded on the nuclear plate and those read at the position 0.33 mm from the left edge (indicated by the dashed line) of the photographs shown in Fig. 4. Figs. 5(*a*1)–5(*a*6) show the intensity profiles of the diffraction from the surface ($P_{\rm h}$) together with those from the lateral surface in the diffracted beam direction ($P_{\rm h}'$). Figs. 5(*b*1)–5(*b*6) show intensity profiles of the diffraction from the back surface ($P_{\rm t}$) and those from the lateral surface in the transmitted beam direction ($P_{\rm t}'$). In Fig. 5, the curves (1), (2), (3), (4), (5) and (6) are intensity profiles when the displacement $D$ is 0, 10, 20, 30, 50 and 70 µm, respectively. There are five interference fringes in $P_{\rm h}'$ when $D$ is changed from 10 µm to 70 µm. Similarly, there are five interference fringes in $P_{\rm t}'$ when $D$ is 10, 20 and 30 µm as shown in Figs. 5(*b*2)–5(*b*4). But for larger $D$ the number of fringes decreases. There are four and three fringes when $D$ is 50 µm (*b*5) and 70 µm (*b*6), respectively. Peaks in $P_{\rm h}'$ and $P_{\rm t}'$ are numbered as peak 1, peak 2 and so on from right to left. Each position of the peaks shifts from the back surface side ($y' = H'$ or $y'' = H''$) to the surface side ($y' = 0$ or $y'' = 0$) both in $P_{\rm h}'$ and $P_{\rm t}'$. Although peak 5 is not clearly seen in either curve (*a*1) or (*b*1) when the crystal is not bent, it appears in the curves (*a*2) and (*b*2) when the strain is applied. The height of peak 5 becomes maximum in curves (*a*3) and (*b*3). The weak peak $P_{\rm h}^{\langle 2\rangle}$ on the left side of $P_{\rm h}'$ in Fig. 5(*a*1) is the intensity of the reflection from the back surface as shown in Fig. 1(*a*). The peak $P_{\rm m}^{\langle 1\rangle}$ on the left side of $P_{\rm h}'$ in Fig. 5(*a*5) is a mirage fringe. The peaks $P_{\rm m}^{\langle 1\rangle}$ and $P_{\rm m}^{\langle 2\rangle}$ in Fig. 5(*a*6) are also mirage fringes. The difference between the origin of the peak $P_{\rm h}^{\langle 2\rangle}$ and that of the peak $P_{\rm h}'$ can be understood by considering the beam trajectories in Fig. 1. The left edge of the peak $P_{\rm h}^{\langle 2\rangle}$ is determined by the beam which is incident on the crystal with the glancing angle $\gamma_{\max}$ and reflected from the back surface shown in Fig. 5(*a*1). This means that $\gamma_{\max}$ can be determined by the left edge position of $P_{\rm h}^{\langle 2\rangle}$. Using the value of $\gamma_{\max}$, the maximum value of the deviation parameter $|W_{\max}|$ can be determined as described below.

## 4. Theoretical analysis

In order to calculate the intensities of mirage fringes, diffraction under a constant strain gradient is considered. The dispersion surface in the two-beam approximation of the dynamical theory of diffraction is given by

$$Y^2 = \frac{X^2}{\tan^2\theta_{\rm B}} - X_0^2, \tag{1}$$

where $\theta_{\rm B}$ is the Bragg angle. The absorption effect is not taken into account. Parameter $X_0$ is given by $X_0 = 1/(2\Lambda)$ with $\Lambda = \lambda\cos\theta_{\rm B}/C|\chi_h|$, where $\lambda$ is the X-ray wavelength, $C$ is the polarization factor and $\chi_h$ is the $h$th Fourier component of the X-ray polarizability. According to Gronkowski & Malgrange (1984), the trajectory of the refracted beam under strain $\beta$ is given by

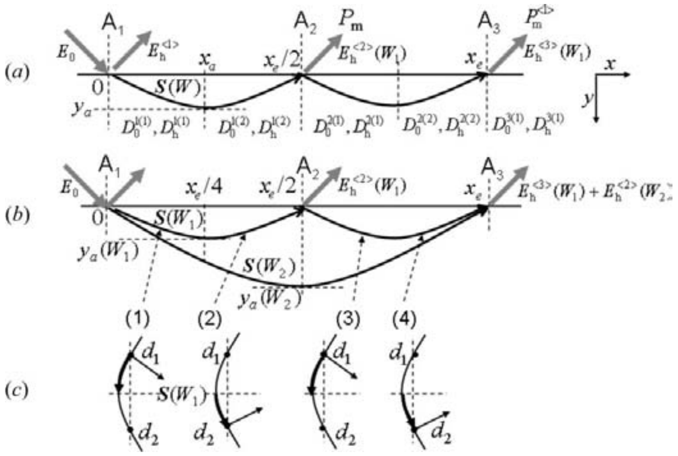

**Figure 6**
Ray trajectories in a bent crystal. (*a*) Ray trajectory of the mirage diffraction. (*b*) Ray trajectories in the mirage fringe. (*c*) Variation of tie points.

$$\left(\frac{\beta y}{\tan\theta_{\rm B}}+W\right)^2-\left[\beta x+s(W)\left(W^2-1\right)^{1/2}\right]^2=1, \qquad (2)$$

using the deviation parameter $W = -X/X_0$. The strain parameter $\beta$ is defined by

$$\beta=\frac{\lambda}{C|\chi_h|\cos\theta_{\rm B}}\frac{\partial^2(\mathbf{h}\cdot\mathbf{u})}{\partial\mathbf{s}_0\partial\mathbf{s}_{\rm h}}, \qquad (3)$$

where $\mathbf{h}$ is the reciprocal lattice vector, $\mathbf{u}$ the displacement vector due to strain, and $\mathbf{s}_0$ and $\mathbf{s}_{\rm h}$ the unit vectors in the transmitted and diffracted beam directions, respectively. In (2), $x$ and $y$ are the coordinates shown in Fig. 6, $s(W)$ is $-1$ for $W < 0$ and $+1$ for $W > 0$.

Fig. 6(*a*) shows the refracted beam trajectory for $W\beta < 0$. The beam is deflected as a result of the strain gradient and comes back to the surface at $A_2$ ($x = x_e/2$) without reflection at the back surface. The vertex of the hyperbolic trajectory in this case is given by

$$x_a=-s(W)\left(W^2-1\right)^{1/2}/\beta, \qquad (4)$$

$$y_a=-(\tan\theta_{\rm B}/\beta)[W-s(W)]. \qquad (5)$$

As $x_a = x_e/4$, $\beta$ can be determined from the position of a mirage fringe. In Fig. 6(*b*) are shown the trajectories of the beams $S(W_1)$ in the $\mathrm{B}\overline{\mathrm{B}}^2$ mode excited at the tie point $(X_1, Y_1)$ and the trajectories of the beams $S(W_2)$ in the $\mathrm{B}\overline{\mathrm{B}}$ mode excited at the tie point $(X_2, Y_2)$. In Fig. 6(*c*) the change of the tie point on the dispersion surface is shown when the refracted beam $S(W_1)$ propagates from $A_1$ to $A_3$ through $A_2$, according to the previous study by Authier (2001). The change in the direction of the refracted beam on the trajectory between $x = 0$ and $x_e/4$ corresponds to the change in the position of the tie point on the $d_1$ side, while the change between $x = x_e/4$ and $x_e/2$ corresponds to the change on the $d_2$ side.

The intensity of the mirage fringe $P_{\rm m}^{\langle 1\rangle}$ is given by

$$I=R_1^2(W_1)+R_2^2(W_2)+2R_1(W_1)R_2(W_2)\cos[2\pi(\Delta\theta_x+\Delta\theta_y)]. \qquad (6)$$

In (6), $R_1(W)$ and $R_2(W)$ are given by using the boundary condition of the electric field on the crystal surface as

$$R_1(W_1)=\frac{E_h^{\langle 3\rangle}(W_1)}{E_0}=-r(W_1)\left[1-r^2(W_1)\right] \qquad (7)$$

and

$$R_2(W_2)=\frac{E_h^{\langle 2\rangle}(W_2)}{E_0}=-\left[1-r^2(W_2)\right]. \qquad (8)$$

Here, $E_h^{\langle 2\rangle}(W_2)$ and $E_h^{\langle 3\rangle}(W_1)$ are the electric fields in the $\mathrm{B}\overline{\mathrm{B}}$ and $\mathrm{B}\overline{\mathrm{B}}^2$ modes, respectively. The reflection coefficient $r(W)$ is defined by $r(W) = D_h^{(1)}/D_0^{(1)}$ with $D_0^{(1)}$ and $D_h^{(1)}$ being the electric displacements of the transmitted and diffracted beams. The superscript (1) means that the beam is excited at a tie point on the $d_1$ side. The phase of the third term in the right-hand side of (6) can be expressed as

$$\Delta\theta=\Delta\theta_x+\Delta\theta_y=\theta_x(W_2)-\theta_x(W_1)+\theta_y(W_2)-\theta_y(W_1). \qquad (9)$$

The phases $\theta_x(W_i)$ and $\theta_y(W_i)$ ($i = 1$ for the $\mathrm{B}\overline{\mathrm{B}}^2$ mode and 2 for the $\mathrm{B}\overline{\mathrm{B}}$ mode) are given by

$$\theta_x(W_i)=2\pi\int k_{0x}\,{\rm d}x=\frac{\pi x_e}{d\tan\theta_{\rm B}}+2\pi M_i\int_0^{x_i}X(W)\,{\rm d}x \qquad (10)$$

and

$$\theta_y(W_i)=2\pi\int k_{0y}\,{\rm d}y=\frac{\pi}{d}M_i y_a(W_i)+2\pi M_i\int_0^{y_a(W_i)}Y(W)\,{\rm d}y, \qquad (11)$$

where $k_{0x}$ and $k_{0y}$ are the $X$ and $Y$ components of the incident wavevector in the crystal. The integrations are carried out along the hyperbolic trajectories of the refracted beams $S(W_1)$ and $S(W_2)$. By considering the fact that $X(W)$ and $Y(W)$ are functions of $x$ and $y$, respectively, the phases can be calculated as

$$\Delta\theta_x=2\pi\left[2\int_0^{x_e/2}X(W)\,{\rm d}x-4\int_0^{x_e/4}X(W)\,{\rm d}x\right] \qquad (12)$$

and

$$\Delta\theta_y=2\pi\left[\Delta m+2\int_0^{y_a(W_2)}Y(W)\,{\rm d}y-4\int_0^{y_a(W_1)}Y(W)\,{\rm d}y\right], \qquad (13)$$

where $\Delta m = m_2 - 2m_1$ with $m_i$ ($i = 1, 2$) being the number of lattice planes given by the relation $2y_a(W_i) = m_i d$ for each refracted beam. The integrations over $x$ and $y$ in (12) and (13) are converted to those over $W$ as

$$\int_0^{xi}X(W)\,{\rm d}x=\mp\frac{X_0}{\beta}\int_{W_i}^{-1}W d\left[(W^2-1)^{1/2}\right] \qquad (14)$$

and

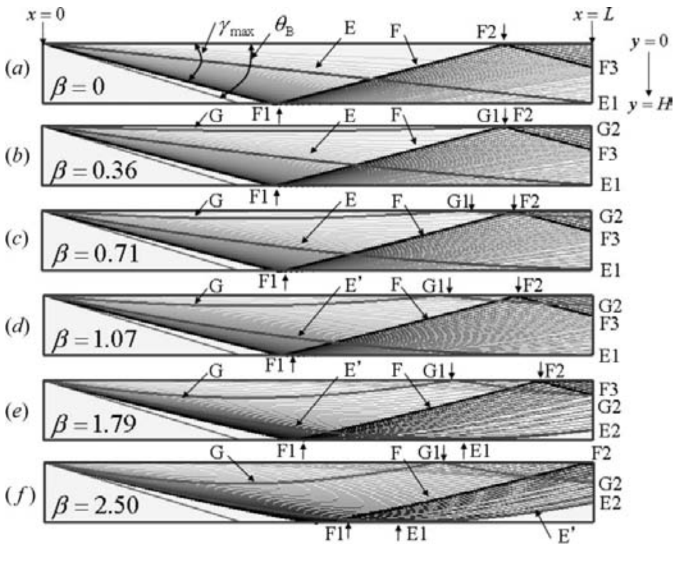

**Figure 7**

Calculated beam trajectories as a function of $W$ between −2.0 and −1.0. The strain $\beta$ is (*a*) 0, (*b*) 0.36, (*c*) 0.71, (*d*) 1.07, (*e*) 1.79 and (*f*) 2.5 mm$^{-1}$. Trajectory E corresponds to the refracted beam reaching to the corner edge ($x = L$, $y = H$) in (*a*)–(*c*) and to the refracted beam coming to the back surface at its vertex ($y_a = H$) in (*d*)–(*f*). Trajectory F corresponds to the refracted beam with the glancing angle $\gamma_{\max}$. Trajectory G corresponds to the beam in the B$\overline{\rm B}$L mode which reaches the lowest position on the lateral surface.

$$\int_0^{ya(W_i)} Y(W)\,{\rm d}y = \pm\frac{X_0}{\beta}\int_{W_i}^{-1}(W^2-1)^{1/2}\,{\rm d}W. \qquad (15)$$

Then once $\beta$ is given, the phases $\Delta\theta_x$, $\Delta\theta_y$ and the intensity $I$ in (6) can be determined. This in turn means that $\beta$ can be determined if the intensity $I$ is known. The dashed curves in Figs. 5(*a*3)–5(*a*6) show the calculated intensities $I$ of equation (6), which reproduce the observed peak positions quite well. For reproducing the two peaks in the observed fringes for $D$ = 70 µm in Fig. 5(*a*6), the value of $\beta$ is assumed to be 2.5 mm$^{-1}$. If $\beta$ is assumed to be proportional to $D$, $\beta$ becomes 1.79 mm$^{-1}$ for $D$ = 50 µm, which reproduces a single peak $P_{\rm m}^{\langle 1\rangle}$ for $D$ = 50 µm as shown in Fig. 5(*a*5). The value of $\beta$ is determined by comparing the calculated curves with the measured curves.

In Fig. 7 the refracted beam trajectories are shown when $W$ is changed from −1 to −2. This range of $W$ is determined by using the maximum value of the glancing angle $\gamma_{\max}$ = 15°. Figs. 7 (*a*)–7(*f*) show the trajectories for different strain $\beta$ = 0, 0.36, 0.71, 1.07, 1.79 and 2.50 mm$^{-1}$, respectively. The trajectory denoted as E is one which reaches the corner edge ($x = L$ and $y = H$) of the crystal. Such a trajectory E exists for $0 < \beta < 1.07$ [Figs. 7(*a*)–7(*c*)]. The trajectory for $\beta$ = 1.07 mm$^{-1}$ (Fig. 7*d*) reaches the corner edge at the vertex of the hyperbola. For $\beta > 1.07$, no trajectory reaches to the corner edge [Figs. 7(*e*)–7(*f*)]. A trajectory coming to the lowest position on the lateral surface without reflection at the back surface (E′) is in contact with the back surface at the vertex of its hyperbolic trajectory ($y_a = H$) and comes out from the crystal at E2. There exists a region (referred to as the 'dark region') below the trajectory E′ in the crystal where no beam trajectory passes. In Figs. 1(*b*) and 1(*c*) the range of the dark region on the lateral surface is denoted as B$_{\rm B}$ and that on the back surface as C$_{\rm B}$. The hatched ranges in Figs. 5(*a*5)–5(*a*6) and (*b*5)–5(*b*6) correspond to dark regions and the intensities in these ranges are quite low. As a result of the dark region, all the peaks in $P'_{\rm h}$ should shift toward $y'$ = 0 and all the peaks in $P'_{\rm t}$ toward $y''$ = 0. These shifts can explain the shifts of the peaks in the measured results. Trajectory F is the trajectory with the glancing angle of the beam $\gamma_{\max}$. The corresponding beam reaches the back surface and is reflected at F1. It reaches the surface at F2 and the lateral surface at F3 as shown in Figs. 7(*a*)–7(*e*). As $\beta$ is increased, the position of F2 shifts to the right. Trajectory G in Figs. 7(*b*)–7(*f*) is the trajectory of the beams which reach the lowest position on the lateral surface in the B$\overline{\rm B}$L mode. Even when the strain is small ($\beta$ = 0.36 mm$^{-1}$), a mirage diffraction should be observed at G1, which corresponds to small peaks in the region indicated by the horizontal arrow in Fig. 5(*a*2).

## 5. Discussion and conclusions

Mirage fringes have been observed in the reflection intensities from the surface of a bent crystal by changing bending strain, as shown in Figs. 5(*a*1)–5(*a*6). The interference fringes have also been observed in the diffraction from the lateral surface. The interference fringes change conspicuously as a function of bending strain as shown in Figs. 5(*b*1)–5(*b*6). The change in both fringes is explained by using the phase factor given in equation (9). The change in the phase is caused by the change in the path length of each refracted beam contributing to the fringes when the bending strain is changed. Such paths under two different values of strain are shown in Figs. 1(*b*) and 1(*c*). The calculated intensities of (6) reproduce the characteristic features such as the number of peaks and the change of the measured fringes in Fig. 5. In Fig. 5(*a*6) two peaks are observed in the mirage fringe when $D$ = 70 µm. Using this fact, the value of $\beta$ is determined to be 2.5 mm$^{-1}$. By using this value and assuming that $\beta$ is proportional to $D$, a peak corresponding to the mirage peak $P_{\rm m}^{\langle 1\rangle}$ as observed in Fig. 5(*a*5) can be reproduced when $D$ = 50 µm as shown by the dashed line. The phase calculation along the beam trajectories by using equation (9) works quite well. Peak 5 is observed only when the bending strain is applied as shown in Fig. 5. This is because the peak 5 is caused by the interference between the beam in the B$\overline{\rm B}$L mode and those in the BL, BBL and BB$^2$L modes as shown in Figs. 7(*b*) and 7(*c*). The increase in height of peak 4 in Figs. 5(*a*4)–(*a*5) is also caused by the interference including the beam in the B$\overline{\rm B}$L mode. In Fig. 5(*a*1), the thin solid line shows the interference intensity between the beam in the BL mode and that in the BBL mode calculated according to the method described by Hirano *et al.* (2008). There are six peaks in the calculation but only four distinct peaks are observed in the measured curve. The positions of peaks 1–4 in the calculation show good agreement with those in the measured curve. However, peaks 5 and 6 obtained in the calculation are not clearly observed in the measured curve. To reproduce diminution or disappearance of peaks 5 and 6 properly, it is necessary to calculate the interference among three beams by taking into account the beam in the BB$^2$L mode. Moreover, for a bent crystal, it is necessary to calculate the interference intensity by including mirage diffraction beams. This will be our future work. The shifts of the peaks in the diffraction from the lateral surface are shown in Figs. 5(*a*5)–5(*a*6) and 5(*b*5)–5(*b*6), which can be explained by extension of the dark region. As the refracted beams in the BL and BBL modes cannot reach the dark region, the beams come out of the crystal only from a restricted area above E2 on the lateral surface shown in Figs. 7(*e*) and 7(*f*). The restricted area decreases as $\beta$ increases, which results in the shift of the interference fringes toward the upper side ($y = 0$) on the lateral surface.

In conclusion, it is pointed out that the changes of the interference fringes and the mirage fringes as a function of the bending strain can be explained by the change of the interference between the beams in multiple BL modes and those of mirage diffraction. The interference changes as the phase factor shifts as a result of the changes in the beam trajectories owing to the strain. This in turn means that the value of the bending strain can be determined by analysing these interference fringes. The analysis based on the dynamical theory of diffraction, especially by the phase factor calculated along the beam trajectories given in equation (9), explains the measured change in interference fringes from the lateral surface as well as mirage fringes from the surface as a function of strain gradient. Recently, Fukamachi *et al.* (2009) have reported an increase in the reflected beam intensity from the surface of a bent crystal when the width of the incident X-rays along the incident azimuth is increased. The intensity increase, *i.e.* the beam density increase, can be explained by addition of the electric fields of the mirage diffraction beam to those of the reflected beams from the surface. The reported beam density gain is approximately four but it will be improved much by using an optimum condition. The mirage diffraction should be quite useful not only for studying the strain gradient in a crystal as shown in this paper but also for designing a monochromator for obtaining highly intense X-ray beams.

The authors thank Professors Masayasu Tokonami and Masayuki Shimojo of Saitama Institute of Technology for valuable discussions. They are grateful to Mrs Yoshinobu Kanematsu and Sukswat Jongsukswat for assistance in some experiments. This work was carried out under the approval of the Program Advisory Committee of PF (proposal No. 2008G545). This work was partly supported by the ‘Open Research Center’ Project for Private Universities: 2007–2009 matching fund subsidy from MEXT (Ministry of Education, Culture, Sports, Science and Technology), and Grant-in-Aid for Scientific Research (c) (19540344) from MEXT.

## References

Authier, A. (2001). *Dynamical Theory of X-ray Diffraction.* Oxford University Press.

Chukhovskii, F. N. & Petrashen’, P. V. (1988). *Acta Cryst.* A**44**, 8–14.

Fukamachi, T., Hirano, K., Yoshizawa, M., Negishi, R., Ju, D., Tohyama, M., Kanematsu, Y., Hirano, K. & Kawamura, T. (2009). *J. Phys. Soc. Jpn*, **78**, 103001.

Fukamachi, T., Negishi, R., Yoshizawa, M. & Kawamura, T. (2005). *Jpn. J. Appl. Phys.* **44**, L787–L789.

Fukamachi, T., Negishi, R., Yoshizawa, M., Sakamaki, T. & Kawamura, T. (2004). *Jpn. J. Appl. Phys.* **43**, L865–L867.

Gronkowski, J. & Malgrange, C. (1984). *Acta Cryst.* A**40**, 507–514.

Hirano, K., Fukamachi, T., Yoshizawa, M., Negishi, R., Hirano, K. & Kawamura, T. (2009*a*). *Acta Cryst.* A**65**, 253–258.

Hirano, K., Fukamachi, T., Yoshizawa, M., Negishi, R., Hirano, K. & Kawamura, T. (2009*b*). *Phys. Status Solidi A*, **206**, 1855–1859.

Hirano, K., Fukamachi, T., Yoshizawa, M., Negishi, R., Hirano, K., Xu, Z. & Kawamura, T. (2008). *J. Phys. Soc. Jpn*, **77**, 103707.

Yan, H., Kalenci, Ö. & Noyan, I. C. (2007). *J. Appl. Cryst.* **40**, 322–331.

Yan, H. & Noyan, I. C. (2006). *J. Appl. Cryst.* **39**, 320–325.

Yoshizawa, M., Fukamachi, T., Hirano, K., Oba, T., Negishi, R., Hirano, K. & Kawamura, T. (2008). *Acta Cryst.* A**64**, 515–518.